Effects of Compressibility on Leading-Edge Dynamic Stall Criteria

Sarasija Sudharsan *1, Shreyas Narsipur^{†2}, and Anupam Sharma^{‡1}

1 Iowa State University, Ames, IA, 50011

2 Mississippi State University, Mississippi State, MS, 39762

The current work evaluates the effectiveness of two leading-edge dynamic stall criteria in mild to moderately compressible regimes using numerical simulations. The two criteria under consideration, namely, the maximum magnitudes of the leading edge suction parameter $(\max(LESP))$ and boundary enstrophy flux $(\max(|BEF|))$, have previously been found to be effective at signaling dynamic stall in the incompressible regime. Based on unsteady Reynolds-averaged Navier-Stokes simulations at a Reynolds number of 2×10^5 and freestream Mach numbers between 0.1 - 0.5, we observe that these criteria are directly applicable in the mild to moderately compressible regimes, since they are reached shortly after suction collapse at the leading edge and well in advance of dynamic stall vortex formation for all the cases. This is attributed to compressibility effects promoting adverse-pressure-gradient(APG)-induced stall for the flow conditions considered. For the highest Mach number of 0.5, shock wave interactions with the separated shear layer are observed. It is noted that although compressibility leads to separation at a lower APG, the maximum APG scaled by the local flow density remains in the same range for all the cases.

I. Introduction

Dynamic stall is the unsteady stall phenomenon that occurs over aerodynamic surfaces undergoing large amplitude transient motion or unsteady maneuvers, for example, over wind turbine or helicopter rotor blades. The modeling and control aspects of dynamic stall have interested aerodynamicists for several decades, since the large, unsteady aerodynamic forces and moments incurred could potentially cause catastrophic structural failure [1, 2]. Stall control efforts are most effective before the formation of the dynamic stall vortex (DSV) [3], a characteristic feature of 'deep' dynamic stall. Therefore, characterizing stall onset is of crucial importance for control efforts to be deployed in a timely manner. Various criteria for dynamic stall onset based on the unsteady aerodynamic coefficients have been explored to formulate first-order, semi-empirical, dynamic stall models [4, 5]. However, the leading edge suction parameter (*LESP*) [6, 7] and the boundary enstrophy flux (*BEF*) have been used to narrow down the identification of stall onset to a finer degree in time [8, 9]. While these two criteria have previously been applied to the incompressible regime, the current work extends their application to compressible flows with freestream Mach numbers, M_{∞} , between 0.1 and 0.5, at a chord-based Reynolds number, Re_c , of 2×10^5 .

Prior studies [1] indicate that compressibility effects become significant in unsteady flows for freestream Mach numbers as low as 0.2. The fundamental mechanisms of dynamic stall are altered by the degree of compressibility, which we have delineated into mild, moderate and highly compressible regimes. In the *mildly-compressible regime*, the flow remains sub-critical, i.e., maximum local flow Mach number over the airfoil, $M_{loc} < 1$. Compressibility promotes adverse-pressure-gradient (APG)-induced leading-edge stall and reduces dynamic-stall delay and dynamic lift overshoot [10]. In the *moderately-compressible regime*, the maximum local flow speed exceeds the sonic speed, but it does not induce shocks strong enough to cause significant boundary layer separation. However, the subsonic flow inside the laminar separation bubble (LSB) can be fully or partially surrounded by the locally-supersonic flow. The stall mechanism here is due to interaction between the LSB and small wave-like disturbances in the surrounding flow [11], which leads to LSB bursting. This fundamentally differs from the APG-induced LSB bursting in the mildly compressible regime. In the *highly-compressible regime*, locally-supersonic flow can produce a complex shock structure (lambda shocks, for instance) near the blade leading edge. Compressibility forces premature boundary layer separation, and the type of shock dictates the trailing-edge boundary layer characteristics - weak shocks thicken the boundary layer,

^{*}Graduate student, Department of Aerospace Engineering, Iowa State University.

[†] Assistant Professor, Department of Aerospace Engineering, Mississippi State University, and Senior Member AIAA.

^{*}Associate Professor, Department of Aerospace Engineering, Iowa State University, and Associate Fellow AIAA.

modest shocks cause local boundary-layer separation followed by reattachment (separation bubble), and strong shocks cause massive trailing-edge flow separation and induce stall [11]. In shock-induced stalls, the flow near the leading edge can remain unaffected even after the boundary layer over the rest of the airfoil is separated and a substantial loss of lift has occurred (see e.g., [12]). These observations are in stark contrast to those observed in the incompressible regime where APG is the primary stall mechanism. For $Re < 10^6$, APG leads to LSB burst and triggers stall, while at higher Re, APG causes flow reversal which grows from the trailing to the leading edge, followed by dynamic stall vortex (DSV) shedding from the leading-edge region, resulting in stall.

In the current work, we examine the effectiveness of two leading-edge stall criteria, namely, $\max(|BEF|)$ and $\max(LESP)$, in indicating compressible dynamic stall onset. We have found them to be effective in the incompressible regime at Re_c 2×10^5 and 3×10^6 [8, 9] where the DSV plays a prominent role in the stall process, regardless of the type of stall observed (leading-edge, mixed or trailing-edge). Both criteria are reached in advance of DSV formation for leading-edge stall with LSB bursting, where trailing-edge separation effects are insignificant. The reason is attributed to the criteria coinciding with the collapse in leading-edge suction due to increasing APG downstream of the suction peak, which triggers LSB bursting, leading to the formation of a DSV. Since compressibility tends to promote APG-induced stall in the mildly compressible regime, we expect that these criteria will be directly applicable in this regime. In the moderately compressible regime, the interaction of shock waves with the separated shear layer and the subsonic flow close to the wall can result in shock-induced flow separation occurring downstream of the leading edge where LESP and BEF are calculated. The current work evaluates these criteria in the mild to moderately compressible regimes using unsteady Reynolds-averaged Navier-Stokes (uRANS) simulations.

II. Methods

We solve the uRANS equations using the open-source code SU2 [13]. We have previously demonstrated [9] that uRANS can capture the trends of *LESP/BEF* variation and the relative instances of events such as lift stall and DSV formation with acceptable accuracy. The compressible Navier-Stokes equations written in strong conservation form are solved by discretization using a finite volume method, with an implicit, second-order, dual-time-stepping [14] approach for time integration. Upwind or central schemes can be used for discretizing the convective fluxes, while central schemes are available for viscous fluxes. SU2 implements several variants of the Menter shear stress transport (SST) and Spalart-Allmaras (SA) turbulence closure models.

Our dataset consists of three uRANS simulations carried out at $Re_c \ 2 \times 10^5$, for an airfoil undergoing a constant-rate, pitch-up motion, pivoted about the quarter-chord point. The three cases are carried out at freestream Mach numbers, M_{∞} , of 0.1, 0.3 and 0.5, respectively. The unsteady motion occurs at a nondimensional pitch rate, $\Omega^* = \Omega_0 c/U_{\infty} = 0.05$, where Ω_0 is the angular velocity of the pitching motion. Static simulations at $\alpha = 4^{\circ}$ are first carried out until a stationary solution is obtained. A smooth, hyperbolic-tangent-based ramp function is prescribed to transition from the static simulation to the final nondimensional pitch rate. Convective fluxes are calculated using the low-dissipation Low Mach Roe (L^2 Roe) [15] model for the two lower Mach numbers, while the classic Roe scheme [16] is used for the highest Mach number simulated. The two-equation SST $k - \omega$ turbulence model (version V2003m) [17], with a freestream turbulence level of 1%, is used for closure.

A structured O-Mesh having 598×180 grid points in the circumferential and radial directions, respectively, was used for all the simulations, with y_+ values less than 1 over the entire airfoil surface. Figure 1 shows different views of the grid used for the simulations. The grid was finalized based on comparisons with prior large-eddy simulations (LES) [8, 18] for the case at $M_{\infty} = 0.1$, which are presented in Appendix A.

III. Results & Discussion

A. Effect of compressibility on stall onset

Compressibility leads to earlier APG-induced, leading-edge stall, attributed to characteristic changes in the transition process near the leading edge [19]. Accordingly, we observe earlier occurrences of moment and lift stall, as shown in Fig. 2, whose top three panels show the variation of unsteady aerodynamic coefficients (C_l, C_d, C_m) with increasing α . The bottom panel shows a point quantity, namely, the maximum value of C_p on the airfoil surface in the first 5% chord near the leading edge, representing peak suction. Peak suction collapse occurs earlier than lift stall; in the time between these two instances, shed vorticity close to the wall organizes into a coherent DSV inducing additional lift over the airfoil surface. However, a progressively weaker DSV is formed as M_{∞} increases, resulting in lower vortex-induced lift

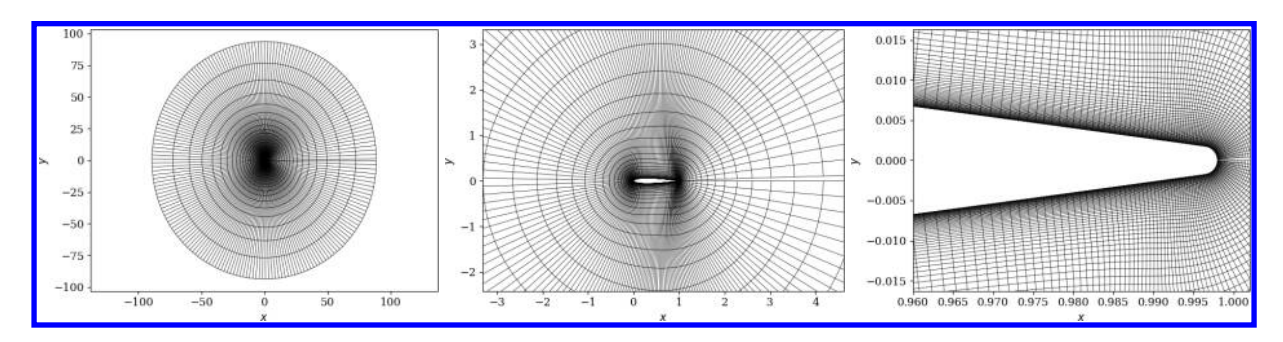


Fig. 1 Grid used in the present study: full view (left), zoomed-in view (middle) and trailing-edge region (right). Every third point in the radial and circumferential directions are shown for clarity in the left and middle panels.

contribution, and smaller divergences in C_d and C_m . Moment stall occurs when the DSV convects past the quarter-chord point and contributes to a nose-down pitching moment. At $M_{\infty}=0.5$, pockets of supersonic flow are observed over the airfoil, with shocks appearing just before the peak suction collapses. The second minimum observed in C_m around 22° for $M_{\infty}=0.5$ corresponds to a trailing-edge vortex that rolls up as the DSV is shed.

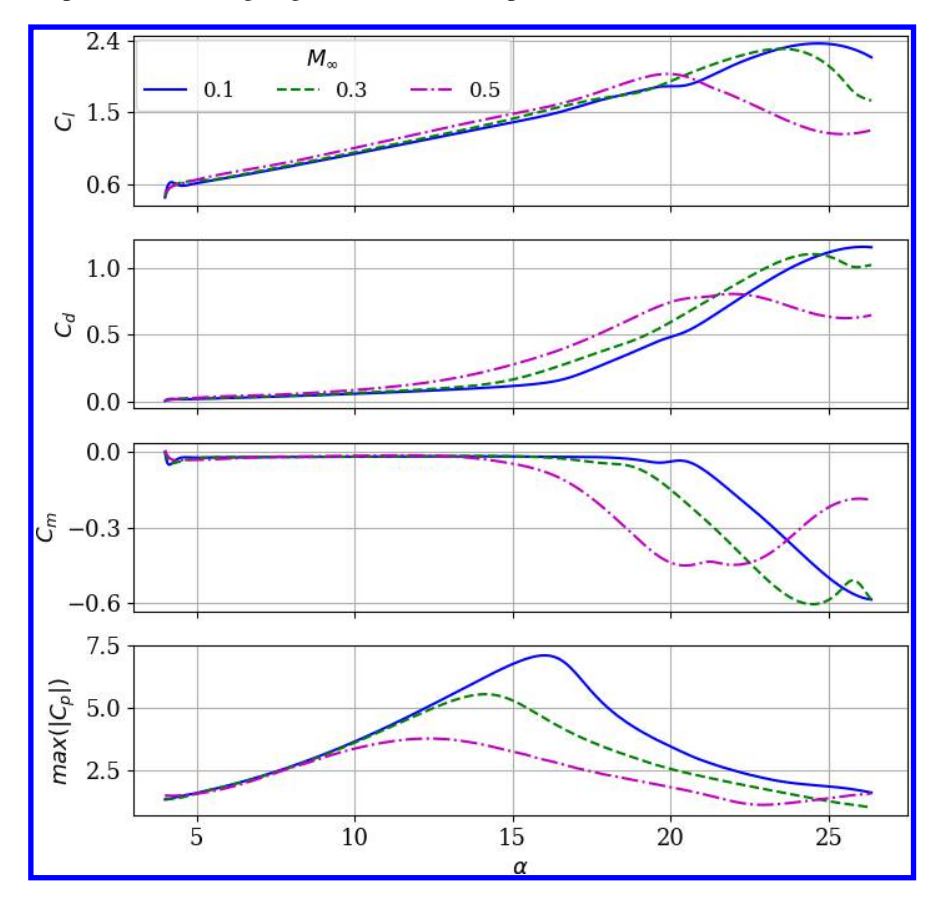


Fig. 2 Variation in unsteady aerodynamic coefficients, C_l , C_d and C_m , and maximum magnitude of C_p near the leading edge as the airfoil pitches up.

The sequence of flow events is illustrated through space-time contours of the pressure coefficient, C_p , and the skin friction coefficient, C_f , over the suction surface. Figure 3 shows these contours at $M_{\infty} = 0.3$. The abscissa corresponds to the normalized chord-wise distance, while the ordinate corresponds to increasing angle of attack, α , in degrees. The increase in peak suction near the leading edge is observed from contours of negative C_p . When the APG following the suction peak reaches a certain magnitude, leading edge flow breaks down, the suction peak collapses, and shed

vorticity organizes itself into a coherent DSV. The DSV propagates downstream (imprint seen from both contours) as α continues to increase, leading to an increase in lift coefficient, even as the peak suction continues to decrease. There is some trailing-edge separated flow that propagates upstream, however, even at its largest extent, it does not extend upstream of 0.6c and there is no interaction with the separated flow at the leading edge. The extent of trailing-edge separation reduces as leading edge stall occurs earlier with increasing M_{∞} .

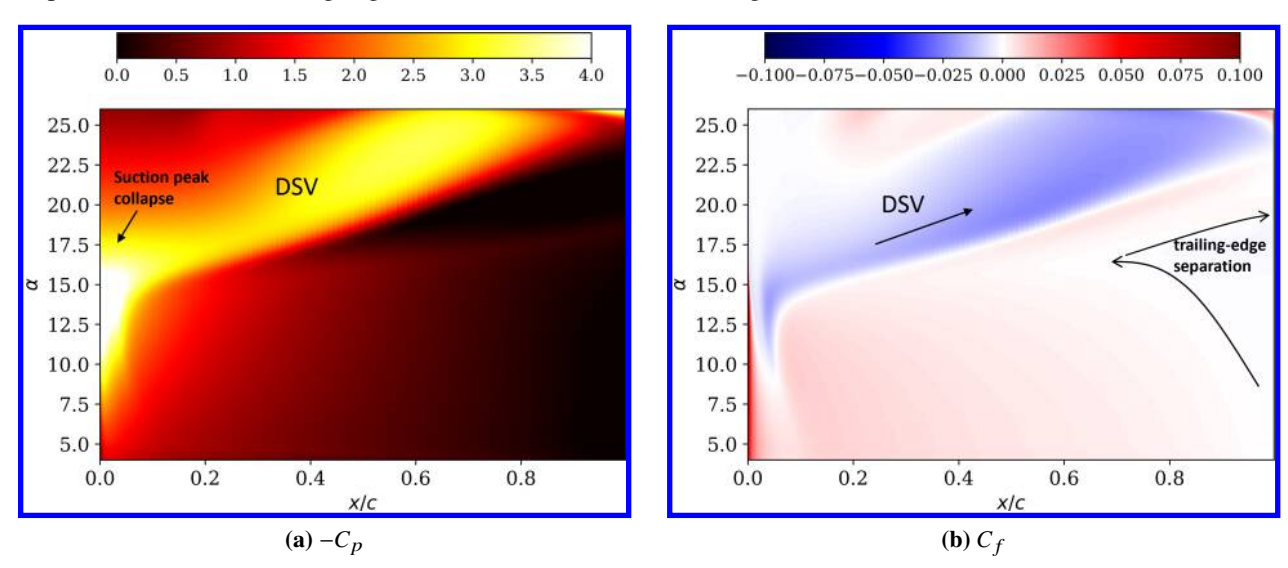


Fig. 3 Space-time contours for the case with $M_{\infty} = 0.3$

Space-time contours of C_p and C_f for the case with $M_{\infty} = 0.5$ are shown in Fig. 4. As the airfoil pitches up, shock waves form closer to the leading edge beginning from about $\alpha = 10.9^{\circ}$ and they interact with the separated shear layer. Suction collapse occurs at a lower α , around 12.3°, with the subsequent formation of a much weaker DSV. The extent of suction near the leading edge is also more spread out in the chordwise direction, compared to $M_{\infty} = 0.3$. This is attributed to a large pocket of supersonic flow that is formed in the region, as shown in Fig. 5a, where there is no information from flow downstream. The top panel of the figure shows streamlines overlaid with local flow Mach number contours and the bottom panel shows the distribution of $-C_p$ over the suction surface. As the separation point of the shear layer moves towards the leading edge and the acceleration over the airfoil reduces, the supersonic pockets reduce in extent and disappear. The DSV is formed in a fully subsonic flow region (Fig. 5b). Note the lack of a large suction peak corresponding to the vortex core. As the DSV is shed and $|C_p|$ drops over most of the airfoil suction surface, a strong counter-clockwise vortex rolls up around the trailing-edge (as pointed out in Fig. 4a). Images of the expansion and shock waves formed near the leading edge above the separated shear layer as the airfoil pitches up are shown in Fig. 6. Contours of $\frac{\mathbf{U}}{a} \cdot \frac{\nabla p}{\|\nabla p\|}$ are shown, where \mathbf{U} , a and p are local values of the velocity vector, sound speed and pressure, respectively, in the airfoil frame of reference. The two instances shown are at $\alpha = 11.1^{\circ}$, just after the shock waves first appear, and at 12.3°, when the peak suction collapses. The development of a stronger shock is seen in panel b of Fig. 6 as flow acceleration around the leading edge continues to increase until suction collapses. Though the shock waves interact with the leading edge shear layer in this case, it does not severely affect the subsonic flow below the shear layer. The general progression of events remains similar to the case at $M_{\infty} = 0.3$, except for the shallower suction profile over the airfoil and the formation of a weaker DSV. Higher-fidelity techniques, such as LES, can help better illuminate the interactions between the shock waves and the shear layer.

Next, we examine the effect of compressibility on the two leading-edge stall criteria, max(|BEF|) and max(LESP).

B. Leading-edge stall criteria

We first provide the definitions of the BEF and LESP parameters; detailed descriptions are available in Refs. [6–8]. For a 2D flow field, the BEF is the flux of the squared spanwise vorticity (ω) at the wall as shown in Eq. (1). ω has been normalized by U_{∞}/c , where U_{∞} is the freestream velocity, and c, the airfoil chord. The normal and tangential directions to the airfoil surface, n and s, respectively, have been normalized by c. The integral is carried out between x/c on the pressure side to x/c on the suction side, with all quantities calculated in the airfoil frame of reference. The inclusion of

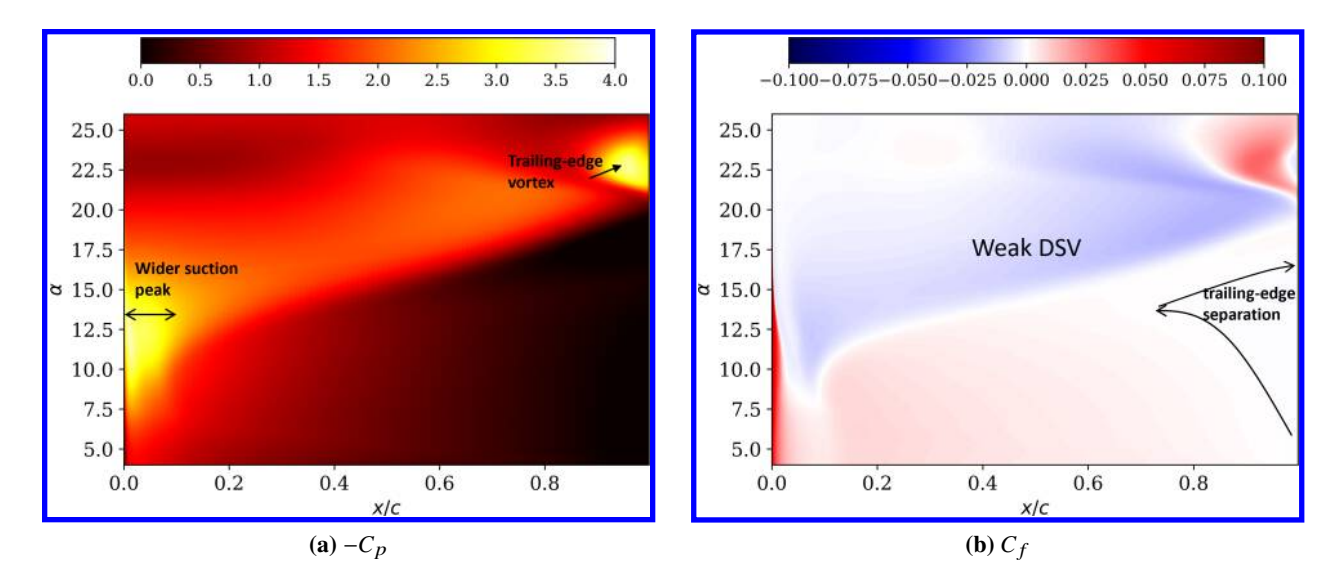


Fig. 4 Space-time contours for the case with $M_{\infty} = 0.5$

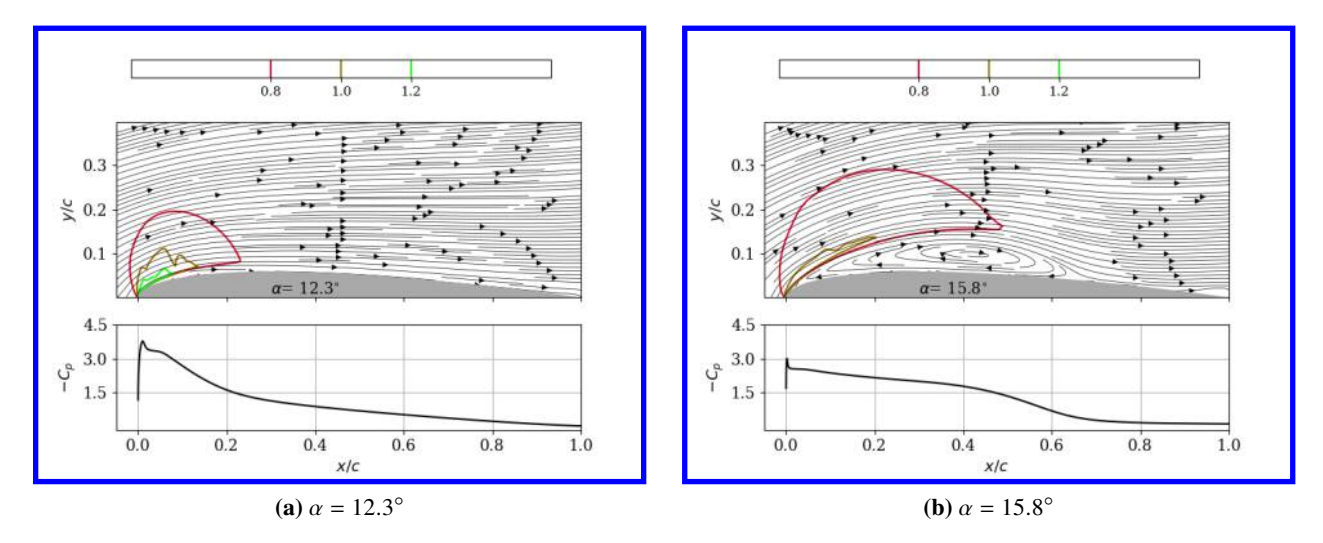


Fig. 5 Supersonic flow above the shear layer at the leading edge (a), and subsonic DSV formation (b). The top panel shows streamlines over the airfoil suction surface overlaid with contours of local Mach number. The bottom panel shows the distribution of $-C_p$ over the airfoil suction surface.

 Re_c is to enable expanding out the integrand, $|\omega^2|$, into a product of vorticity and boundary vorticity flux scaled by Re_c , which is equivalent to the favorable pressure gradient for small tangential acceleration. Large contributions to the BEF arise only from regions of high vorticity combined with large pressure gradients, which is primarily the leading-edge region. The BEF is therefore nearly independent of integration length, as long the region very close to the leading edge (about 1% chord based on prior studies [8]) is included.

$$BEF = \frac{1}{Re} \int_{(x/c)_p}^{(x/c)_s} \omega \frac{\partial \omega}{\partial n} ds$$
 (1)

LESP, given by Eq. (2), is a measure of the camber-wise suction force $(F_{s,LE})$ near the leading edge, obtained by integrating the pressure coefficient C_p . q_∞ is the freestream dynamic pressure. The integral to calculate the force is carried out from the maximum thickness point on the pressure side to that on the suction side.

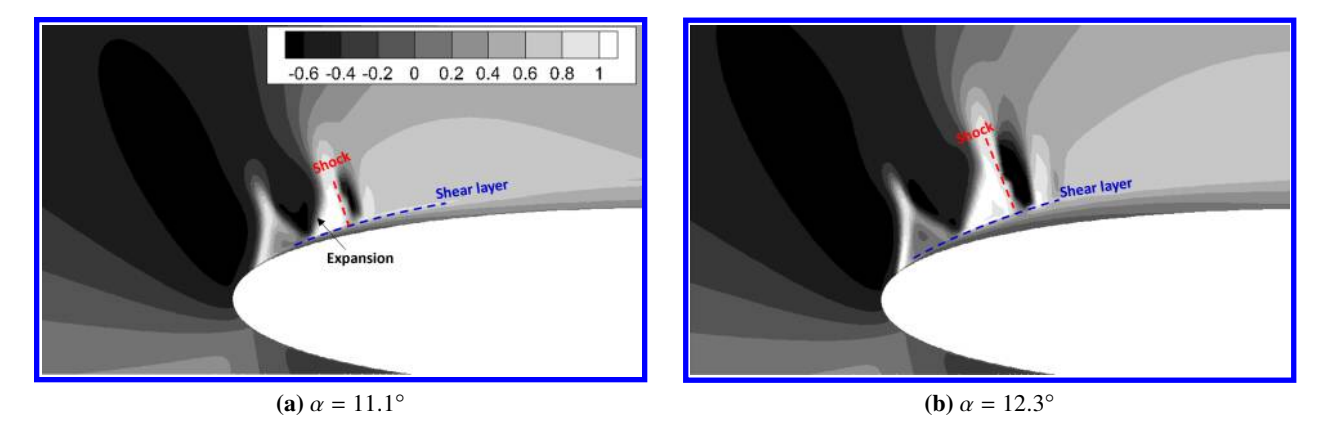


Fig. 6 Shock contours $(\frac{\mathbf{U}}{a} \cdot \frac{\nabla p}{\|\nabla p\|})$ over the airfoil just after the first occurrence (a) and at the instance of leading-edge suction collapse (b).

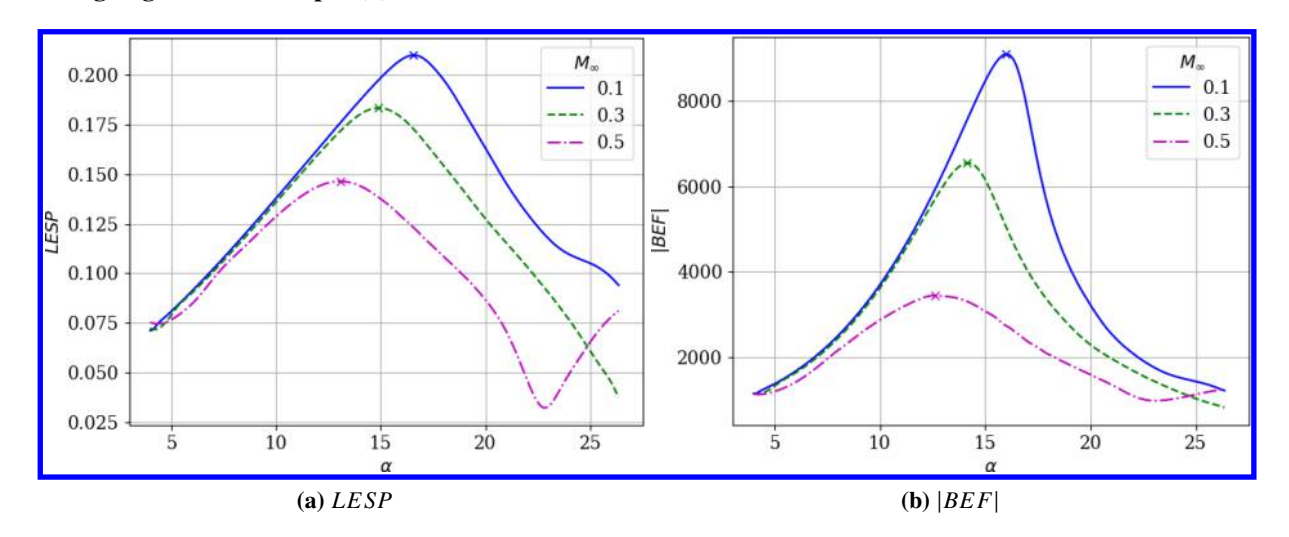


Fig. 7 Variation of the leading-edge stall criteria, LESP and BEF, with α .

$$LESP = \sqrt{\frac{C_{s,LE}}{2\pi}}, \text{ where } C_{s,LE} = F_{s,LE}/q_{\infty}c,$$
 (2)

Next, we compare the variation of the two leading-edge criteria, LESP and |BEF|. The instance of $\max(|BEF|)$ occurs exactly or immediately after peak suction collapse for all the cases. The reason for the BEF, an integrated quantity, closely mimicking the peak suction, a point quantity, is explained in detail in Sudharsan et al. [8]. The instance of $\max(LESP)$ follows within about $0.5 - 0.7^{\circ}$ of $\max(|BEF|)$ for all the cases. DSV formation occurs between $2 - 4^{\circ}$ after the stall criteria are reached, as found from examining C_P distributions and streamlines over the airfoil. Therefore, based on the current results, these criteria are suitable for direct application in the mild to moderate compressible regimes. Their extension to moderate to highly compressible regimes requires further analysis with cases where severe shock-induced separation occurs. Relative to LESP, the BEF is much more sensitive to vorticity accumulation signaling imminent vortex formation, as observed from the pointed peaks for the lower Mach number cases. However, since suction collapse occurs after the formation of supersonic regions near the leading edge for the $M_{\infty} = 0.5$ case, the peak of |BEF| is shallower (as is that of $\max(|C_P|)$ in the bottom panel of Fig. 2).

C. Note on maximum APG

It has been noted in the literature [11, 19] that compressibility reduces the peak APG that the flow can withstand at the leading edge, leading to separation at lower APG at high M_{∞} . This is corroborated by the present results as shown in

Fig. 8a, which plots the maximum APG (point quantity) following the suction peak versus α for all the cases. However, when the maximum of the APG scaled by local density is considered, the peak values all lie in the same range, as shown in Fig. 8b. This could prove useful in future studies as a compressibility correction to find a critical APG for stall onset.

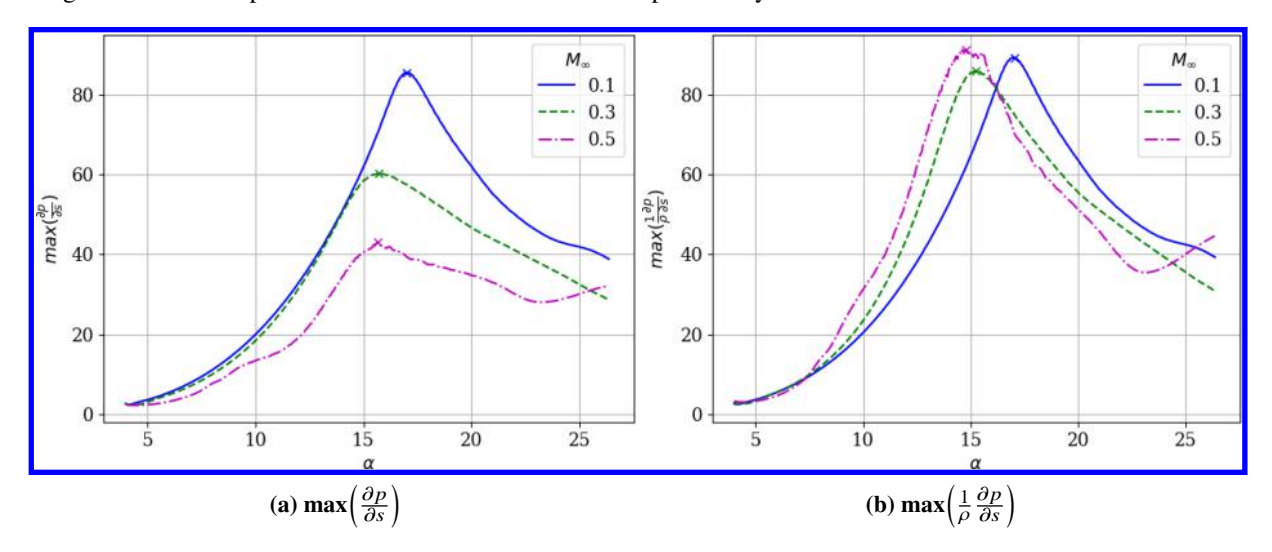


Fig. 8 Variation of maximum APG following the suction peak (a) and maximum of APG scaled by local flow density (b) as α increases.

IV. Conclusion

The effectiveness of leading-edge dynamic stall criteria (max(|BEF|) and max(LESP)) in the mild to moderately compressible regimes was considered in the present work. Based on uRANS simulations at $Re_c \ 2 \times 10^5$ and M_{∞} between 0.1 - 0.5, we observe that these criteria are directly applicable, since they are reached shortly after suction collapse and well in advance of DSV formation. This is attributed to compressibility effects promoting APG-induced stall under the flow conditions considered. For the highest Mach number case of $M_{\infty} = 0.5$, shock wave interactions with the separated shear layer are observed. Though the shear layer is perturbed by the shock waves, the flow beneath the shear layer is not strongly affected. The use of higher-fidelity techniques such as LES can help to illuminate the nature of these interactions. At higher M_{∞} , it is possible to have strong shock wave-shear layer interactions that can result in shock-induced separation, where these criteria are yet to be evaluated. These could be considered in future studies. As a final observation, we noted that though compressibility leads to separation at a lower APG, the maximum APG scaled by the local flow density remains in the same range for all the cases.

Acknowledgements

Funding for this research is provided by the National Science Foundation (grants CBET-1554196 and 1935255). Co-author Sharma acknowledges the support provided to him by the 2019 and 2021 AFOSR Summer Faculty Fellowships. Computational resources are provided by the National Science Foundation (grant MRI-2018594) and the Argonne Leadership Computing Facility, which is a DOE Office of Science User Facility supported under Contract DE-AC02-06CH11357.

Appendix

A. Comparison with LES

Figure 9 compares the unsteady aerodynamic coefficients between LES (black, solid) and uRANS (pink, dashed) for the case with $M_{\infty} = 0.1$. Detailed descriptions of the LES are available in Refs. [8, 18]. We see that the peak values of the coefficients occur slightly later for uRANS. Also, finer variations in the coefficients due to small-scale structures that are generated are not captured in uRANS, as expected. However, the overall match in terms of magnitudes and trends of

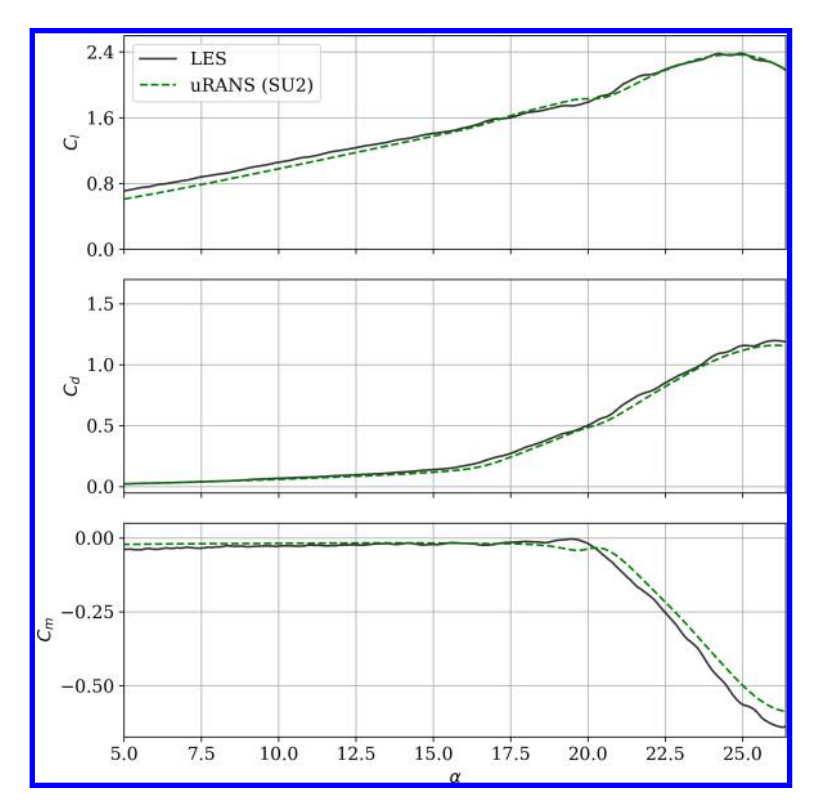


Fig. 9 Comparison of unsteady aerodynamic coefficients between LES and uRANS for $M_{\infty} = 0.1$.

the aerodynamic coefficients is quite good.

Figure 10 compares the variation of LESP and |BEF| between LES and uRANS. For both parameters, uRANS overpredicts the maximum value and shifts it aft by about $0.4 - 0.6^{\circ}$, so we present their variation normalized by the maximum value of each. Our primary interest is in capturing the trend of the variation, which is achieved by uRANS. Therefore, for the present purposes, i.e., identifying the $\max(LESP)$ and $\max(|BEF|)$ criteria relative to DSV formation, we only consider their peak locations in time. The slight shifts in the peaks of the quantities between LES and uRANS are acceptable since there is a corresponding aft shift in time for all other events, such as peak suction collapse and DSV formation. We therefore utilize uRANS for evaluating the above criteria for the considered cases.

Figure 11 compares the space-time contours of C_f between LES and uRANS. The contours corresponding to LES capture small-scale features, while the uRANS results are smoothed out since such features are not captured. However, features such as DSV propagation and trailing edge separation and reattachment are broadly captured well, though there is a slight shift aft in α for the uRANS cases. We find this to be acceptable for the purpose of relative comparisons of the stall onset criteria with the critical points such as peak suction collapse and DSV formation.

References

- [1] McCroskey, W. J., "The phenomenon of dynamic stall," Tech. rep., NASA, Washington, DC, 1981.
- [2] Corke, T. C., and Thomas, F. O., "Dynamic Stall in Pitching Airfoils: Aerodynamic Damping and Compressibility Effects," Annual Review of Fluid Mechanics, Vol. 47, No. 1, 2015, pp. 479–505. https://doi.org/10.1146/annurev-fluid-010814-013632, URL http://www.annualreviews.org/doi/10.1146/annurev-fluid-010814-013632.
- [3] Chandrasekhara, M. S., "Compressible dynamic stall vorticity flux control using a dynamic camber airfoil," *Sadhana*, Vol. 32, 2007, pp. 93–102. https://doi.org/10.1007/s12046-007-0008-8, URL https://doi.org/10.1007/s12046-007-0008-8.
- [4] Leishman, J. G., and Beddoes, T. S., "A Semi-Empirical Model for Dynamic Stall," *J. Am. Helicopter Soc.*, Vol. 34, 1989, pp. 3–17.
- [5] Sheng, W., Galbraith, R. A. M., and Coton, F. N., "A New Stall-Onset Criterion for Low Speed Dynamic-Stall," Journal of

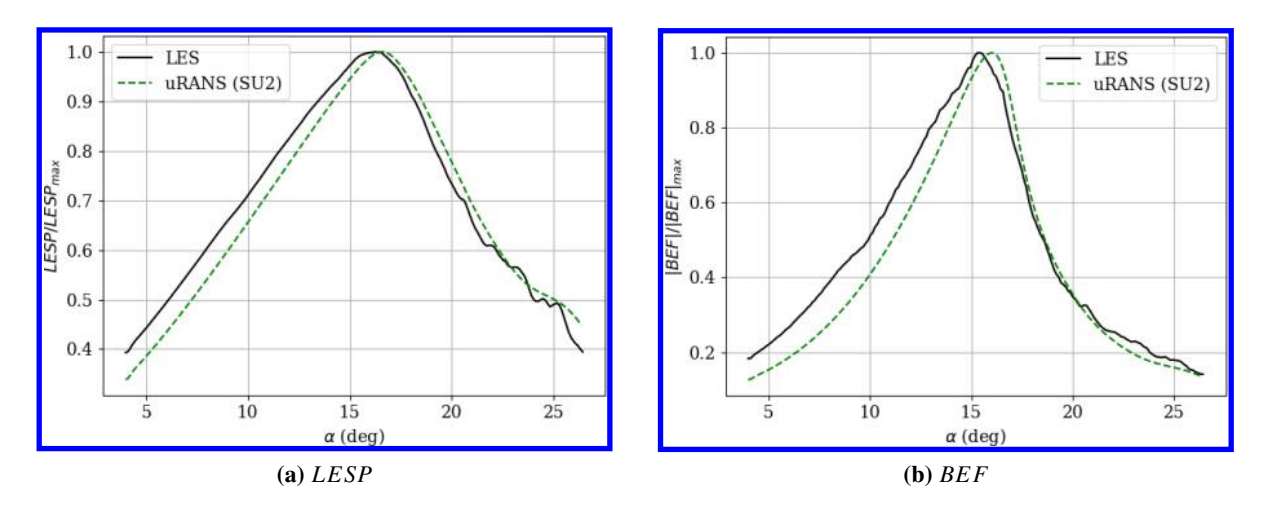


Fig. 10 Comparison of LESP (a) and |BEF| (b) from LES and uRANS normalized by their maximum values for $M_{\infty}=0.1$.

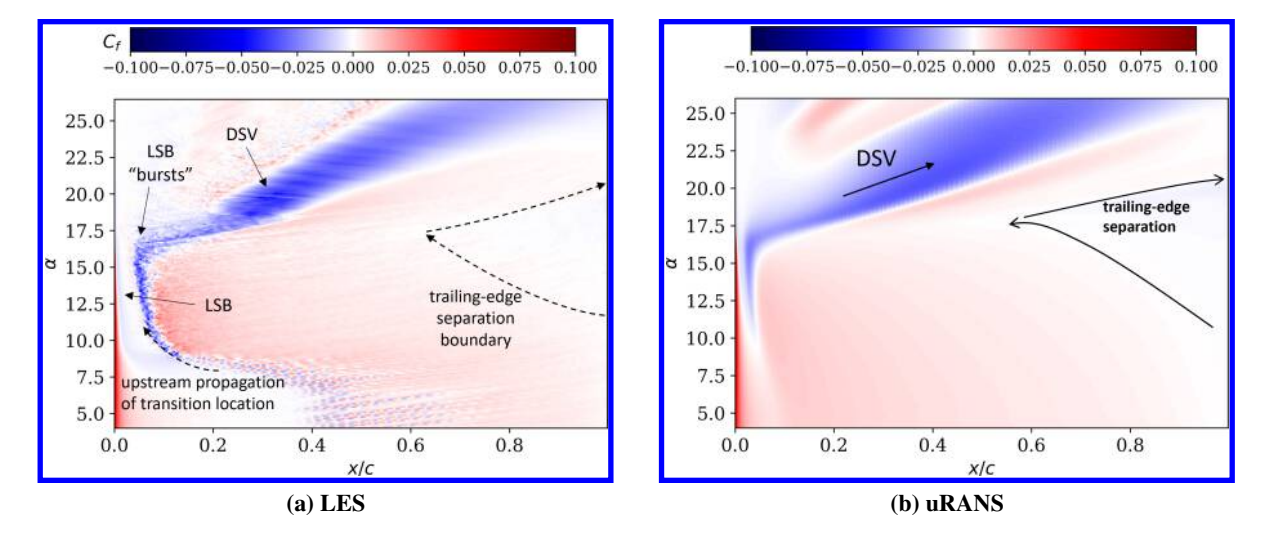


Fig. 11 C_f space-time contours from LES (a) and uRANS (b) for $M_{\infty} = 0.1$.

- Solar Energy Engineering, Vol. 128, No. 4, 2005, pp. 461–471. https://doi.org/10.1115/1.2346703, URL https://doi.org/10.1115/1.2346703.
- [6] Ramesh, K., Gopalarathnam, A., Granlund, K., Ol, M. V., and Edwards, J. R., "Discrete-vortex method with novel shedding criterion for unsteady aerofoil flows with intermittent leading-edge vortex shedding," *Journal of Fluid Mechanics*, Vol. 751, 2014, p. 500–538. https://doi.org/10.1017/jfm.2014.297.
- [7] Narsipur, S., Hosangadi, P., Gopalarathnam, A., and Edwards, J. R., "Variation of leading-edge suction during stall for unsteady aerofoil motions," *Journal of Fluid Mechanics*, Vol. 900, 2020, p. A25. https://doi.org/10.1017/jfm.2020.467.
- [8] Sudharsan, S., Ganapathysubramanian, B., and Sharma, A., "A vorticity-based criterion to characterise leading edge dynamic stall onset," *Journal of Fluid Mechanics*, Vol. 935, 2022, p. A10. https://doi.org/10.1017/jfm.2021.1149.
- [9] Sudharsan, S., Narsipur, S., and Sharma, A., "Evaluating Dynamic Stall-Onset Criteria for Mixed and Trailing-Edge Stall," *AIAA Journal*, Vol. 61, No. 3, 2023, pp. 1181–1196. https://doi.org/10.2514/1.J062011, URL https://doi.org/10.2514/1.J062011.
- [10] Carr, L. W., and Chandrasekhara, M. S., "Compressibility effects on dynamic stall," *Progress in Aerospace Sciences*, Vol. 32, No. 6, 1996, pp. 523–573. https://doi.org/https://doi.org/10.1016/0376-0421(95)00009-7, URL https://www.sciencedirect.com/science/article/pii/0376042195000097.
- [11] Chandrasekhara, M. S., Wilder, M. C., and Carr, L. W., "Competing mechanisms of compressible dynamic stall," AIAA, Vol. 36, No. 3, 1998, pp. 387–393.
- [12] Dadone, L. U., "Two-dimensional wind tunnel test of an oscillating rotor airfoil, volume 1," Tech. Rep. NASA Contractor Report 2915, 1977.
- [13] Economon, T. D., Palacios, F., Copeland, S. R., Lukaczyk, T. W., and Alonso, J. J., "SU2: An Open-Source Suite for Multiphysics Simulation and Design," AIAA Journal, Vol. 54, No. 3, 2016, pp. 828–846. https://doi.org/10.2514/1.J053813, URL https://doi.org/10.2514/1.J053813.
- [14] Jameson, A., "Time dependent calculations using multigrid, with applications to unsteady flows past airfoils and wings," *10th computational fluid dynamics conference*, 1991, p. 1596.
- [15] Oßwald, K., Siegmund, A., Birken, P., Hannemann, V., and Meister, A., "L2Roe: a low dissipation version of Roe's approximate Riemann solver for low Mach numbers," *International Journal for Numerical Methods in Fluids*, Vol. 81, No. 2, 2016, pp. 71–86.
- [16] Roe, P. L., "Approximate Riemann solvers, parameter vectors, and difference schemes," *Journal of computational physics*, Vol. 43, No. 2, 1981, pp. 357–372.
- [17] Menter, F. R., Kuntz, M., and Langtry, R., Ten Years of Industrial Experience with the SST Turbulence Model, Begell House, Inc., 2003, pp. 625–632.
- [18] Sharma, A., and Visbal, M., "Numerical investigation of the effect of airfoil thickness on onset of dynamic stall," *Journal of Fluid Mechanics*, Vol. 870, 2019, p. 870–900. https://doi.org/10.1017/jfm.2019.235.
- [19] Benton, S. I., and Visbal, M. R., "Effects of compressibility on dynamic-stall onset using large-eddy simulation," *AIAA*, Vol. 58, No. 3, 2020, pp. 1194–1205.